Direct Imaging of Dopant Clustering in Metal–Oxide Nanoparticles

Marta D. Rossell,[*,†,‡] Quentin M. Ramasse,[§] Scott D. Findlay,[⊥] Felix Rechberger,[‡] Rolf Erni,[†] and Markus Niederberger[‡]

[†]Electron Microscopy Center, Empa, Swiss Federal Laboratories for Materials Science and Technology, 8600 Dübendorf, Switzerland, [‡]Department of Materials, ETH Zürich, 8093 Zürich, Switzerland, [§]SuperSTEM Laboratory, STFC Daresbury Campus, Warrington, WA4 4AD, United Kingdom, and [⊥]School of Physics, Monash University, Victoria 3800, Australia

ABSTRACT

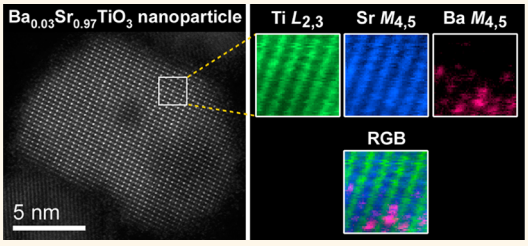

Dopant atoms are used to tailor the properties of materials. However, whether the desired effect is achieved through selective doping depends on the dopant distribution within the host material. The clustering of dopant atoms can have a deleterious effect on the achievable properties because a two-phase material is obtained instead of a homogeneous material. Thus, the examination of dopant fluctuations in nanodevices requires a reliable method to chemically probe individual atoms within the host material. This is particularly challenging in the case of functionalized nanoparticles where the characteristic length scale of the particles demands the use of a high-spatial-resolution and high-sensitivity technique. Here we demonstrate a chemically sensitive atomic resolution imaging technique which delivers direct site-specific information on the dopant distribution in nanoparticles. We employ electron energy-loss spectroscopy imaging in a scanning transmission electron microscope combined with multivariate statistical analysis to map the distribution of Ba dopant atoms in $SrTiO_3$ nanoparticles. Our results provide direct evidence for clustering of the Ba dopants in the $SrTiO_3$ nanoparticles outlining a possible explanation for the presence of polar nanoregions in the Ba:$SrTiO_3$ system. The results we present constitute the first example of site-specific atomic resolution spectroscopy of foreign atoms in doped nanoparticles and suggest a general strategy to ascertain the spatial distribution of impurity atoms in nanocrystals and hence improve the performance of nanoparticle-based devices.

KEYWORDS: dopant atoms · cluster formation · metal-oxide nanoparticles · electron energy-loss spectroscopy · scanning transmission electron microscopy

Nanoparticles hold enormous potential for applications in fields as diverse as catalysis, sensors, magnetic devices, optoelectronics, spintronics, flat panel display technology, and biomedical imaging. A powerful method to control and tailor the properties of nanoparticles is the use of dopant atoms.[1,2] However, fluctuations of the dopant distribution may alter the desired effect and thus impact the performance and reliability of nanoparticle-based devices. Hence, chemical information on doped nanoparticles is essential to understand the diffusion and segregation phenomena of individual dopant atoms and their implications for the functionality of these devices. But it is still a major challenge to directly characterize the distribution of individual dopant atoms in nanocrystals.

A few spectroscopic methods that are sensitive to some physical property specific to the dopants themselves have been used to analyze the local site symmetry and electronic structure of impurities.[3] For example, electron paramagnetic resonance and optical absorption spectroscopy respectively reveal spin interactions and electronic transitions that are sensitive to the local environment of the impurity. Other examples of analytical techniques sensitive to dopant atoms are X-ray spectroscopy, Rutherford backscattering, photoluminescence, and infrared spectroscopy. However, these are statistical methods that probe several hundreds or thousands of nanostructures. Consequently, the data obtained may be an average over many individual nanostructures with significant statistical variations. Thus, these techniques fall short of giving local structural information at the atomic scale.

Currently, the most advanced techniques for observing single impurities are optical spectroscopy especially for nitrogen-vacancy centers in diamond, transport spectroscopy in silicon metal-oxide-semiconductor field-effect transistors, and cross-sectional scanning tunneling microscopy for impurities in III–V and II–VI materials.[4] Yet, each of these techniques is particularly suited for selective impurity–host combinations, and unsuitable for others. Moreover, there remains a central problem: how to determine the

* Address correspondence to marta.rossell@empa.ch.

Received for review May 14, 2012 and accepted July 2, 2012.

Published online July 02, 2012
10.1021/nn3021212

chemical nature of the probed impurity. Its solution requires an imaging technique with single-atom chemical sensitivity.

Transmission electron microscopy (TEM) provides the spatial resolution to study the structure of materials on the atomic level. Because of its favorable atomic-number contrast, scanning transmission electron microscopy (STEM) with a high-angle annular dark-field (HAADF) detector has widely been used to directly image individual impurities inside a crystalline matrix,[5−12] at interfaces,[13] within the lattice of two-dimensional materials,[14] and recently even in the pores of beam sensitive zeolites.[15,16] Apart from the actual image information, STEM is ideally suited for simultaneous imaging and spectroscopy: the transmitted electrons can be collected by a HAADF detector to form an atomic-number (*Z*-) contrast image and by an on-axis electron energy-loss spectrometer to collect direct chemical information of the atomic species that inelastically interact with the electron beam when undergoing an excitation of a core electron. Provided the size of the incident electron probe is small enough, electron energy-loss spectroscopy (EELS) can be performed with atomic resolution.[17] Moreover, the STEM-EELS technique enables the detection and identification of individual atoms[18] and the ability to map the elemental distribution at atomic resolution. Two-dimensional EELS mapping was demonstrated by Okunishi *et al.*[19] and later on explored by, Kimoto *et al.*,[20] Bosman *et al.*[21] and Muller *et al.*[22] However, relatively few studies of doped nanocrystals have been reported, and there are even fewer that combine direct imaging with spectroscopic identification of individual dopant atoms in nanoparticles.[23]

Here, we investigate the spatial distribution of barium atoms in 3 atom %-Ba doped $SrTiO_3$ (STO) nanocrystals employing STEM-EELS imaging combined with multivariate statistical analysis[24] and image simulations of the HAADF and EELS signals. At low temperatures, the chemically pure STO is known to exhibit quantum paraelectricity featured by high dielectric permittivity and low dielectric loss.[25] However, the occurrence of a ferroelectric transition in STO is suppressed by quantum fluctuations.[26] An approach to suppress the intrinsic quantum fluctuations and to induce ferroelectric transitions is to substitute Sr^{2+} by isovalent polar impurities such as Ca^{2+}, Ba^{2+}, and Pb^{2+}.[27]

RESULTS AND DISCUSSION

Crystalline Ba (3 atom %)-doped STO perovskite nanoparticles with Sr and Ti as the A- and B-site cations, respectively, were obtained with the use of a nonhydrolytic and halide-free procedure.[28] The sample consisted of dispersed nanoparticles typically exhibiting

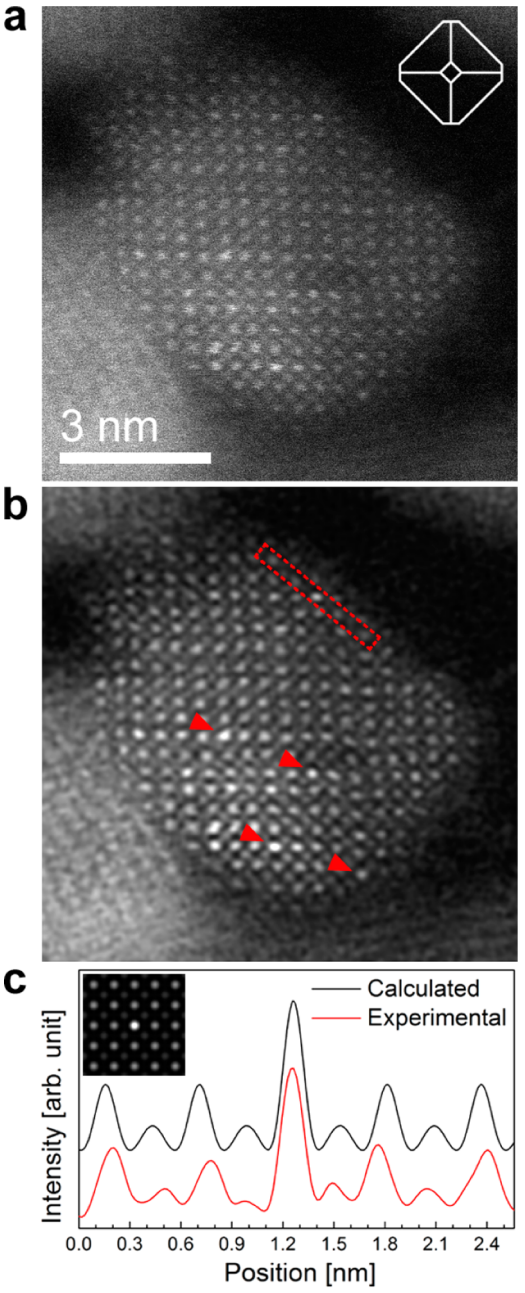

Figure 1. Imaging Ba dopant atoms in Ba-doped STO nanoparticles. (a) HAADF-STEM micrograph of a Ba-doped STO nanoparticle oriented along [001] with an inset showing good agreement with the truncated octahedral shape. (b) Processed image using a smooth low-pass filter set at a spatial frequency corresponding to 0.16 nm to reduce the high-frequency noise. Arrowheads indicate the presence of substitutional heavy Ba atoms in Sr positions. (c) Intensity profile taken along the region outlined with a box in panel b and calculated HAADF-STEM profile of a 0.4 nm thick STO crystal containing a substitutional Ba atom. Inset: corresponding simulated HAADF image.

(truncated) octahedron morphologies with sizes between 3 and 30 nm. A high-resolution STEM image of such a doped STO particle oriented along a cubic axis is shown in Figure 1a. This micrograph was obtained with a conventional STEM/TEM microscope which enables a large depth of field combined with an

excellent *Z*-contrast where the HAADF signal approximately scales with the square of the atomic-number (Z) and the thickness of the sample. Qualitatively, two types of atomic columns are present in the particle of Figure 1a: the bright dots correspond to Sr columns while the weaker dots in between are TiO columns. As the atomic number of Ba is larger than any of the other elements present, columns containing Ba ions are readily observable as occasional higher intensity columns both at the edges and the center of the nanoparticle; see Figure 1b. Such intensity variations on the A-site columns were never observed in nondoped-STO nanoparticles. Note that no Ba atoms are found to form clusters on the surface of the nanoparticles. An intensity profile extracted along a ⟨110⟩-type direction parallel to the edge of the nanoparticle is shown in Figure 1c. No intensity variations due to sample thickness are expected along this row of atom columns. The intensities of the Sr and TiO columns are uniform except for one high intensity column in the center. This atomic column contains a substitutional Ba atom showing an intensity rise of ~175% compared to the average intensity of the neighboring Sr columns. This observation is in good agreement with a corresponding HAADF-STEM image simulation of a crystal consisting of 5 × 5 × 1 STO unit-cells where one Sr atom is exchanged by a Ba atom.

HAADF images were also simulated for 1.2, 2.3, and 3.9 nm thick crystals, corresponding to 3, 6, and 10 unit cells, respectively; see Figures 2a–c. Single-pixel line profiles across the calculated HAADF images at the positions indicated by boxes are shown in Figure 2e. These simulations demonstrate that under the present observation conditions the experimentally observed strong spots are likely to be dopant atoms. However, the simulations reveal that for a Sr column containing a single Ba atom to be more than 25% brighter than a pure Sr column, the sample must be thinner than 2.3 nm (i.e., 6 unit cells). Regarding the noise in the experimental data, this value can be considered as an upper detection limit. Hence, the weak scattering of electrons by single impurity atoms is a serious limitation of the HAADF-STEM technique. Especially for particles larger than 2 nm in diameter, the image signal generated from (quasi-)elastic electron scattering of the buried Ba impurity atoms is hidden in the dominant bulk STO signal, rendering the dopant atoms undetectable. In order to be able to detect individual Ba atoms in thicker areas of the nanocrystals, a chemically specific imaging technique, such as EELS mapping, must be used.

The STEM-EELS data in Figure 3, which was obtained by using a dedicated aberration-corrected scanning transmission electron microscope, depict a HAADF-STEM image of a ~13 nm diameter doped STO particle oriented along the [011] direction. The corresponding EELS spectrum images in Figures 3b–d were acquired

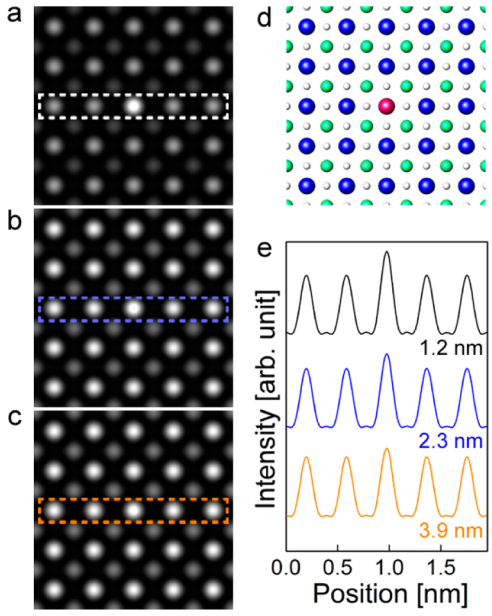

Figure 2. *Z*-contrast STEM image simulations of a Ba atom in STO. (a–c) Simulated HAADF-STEM images calculated respectively for 1.2, 2.3, and 3.9 nm thick STO crystals where one Sr atom was exchanged by a Ba atom at the entrance side of the electron beam. (d) Rendering of the supercell with the Ba atom in the center. Ba, Ti, Sr, and O atoms are depicted as red, green, blue, and white spheres, respectively. (e) Single-pixel line profiles across the atom rows marked by rectangles in panels a–c.

simultaneously with HAADF images from the areas marked with boxes in Figure 3a. The raw EELS data were processed by principal component analysis using multivariate statistical analysis.[24] After noise reduction by multivariate statistical analysis, the background in all spectra was subtracted by fitting a decaying exponential function to an energy window just in front of the different core-loss edge onsets. Figure 3 panels b–d show the elemental atomic-resolution maps of the Ti $L_{2,3}$, Sr $M_{4,5}$, O K, and Ba $M_{4,5}$ edges (see Supporting Information Figure S1) extracted from the spectrum images. These results demonstrate that the Sr and Ba signals largely correlate, consistent with the idea that Ba substitutes at Sr sites. While the Ti, Sr, and O intensities are relatively homogeneous through the images, the Ba maps show significant spatial variations in the distribution of the dopant atoms. Ba atoms have a distinct tendency to form $BaTiO_3$ (BTO) nanodomains in STO, although isolated Ba atoms are also observed in Figure 3 panels c,d. Exactly the same fluctuation patterns are observed in the corresponding atomic-resolution maps of the Ba $N_{4,5}$ edge (see Supporting Information Figure S2). Similar results were obtained for other nanoparticles oriented along the [001] and [011] zone axes.

It could be argued that the signal arising from the core-loss events is not sufficiently localized to directly interpret the maps and that the observed BTO clusters are most likely artifacts caused by electrons transferred

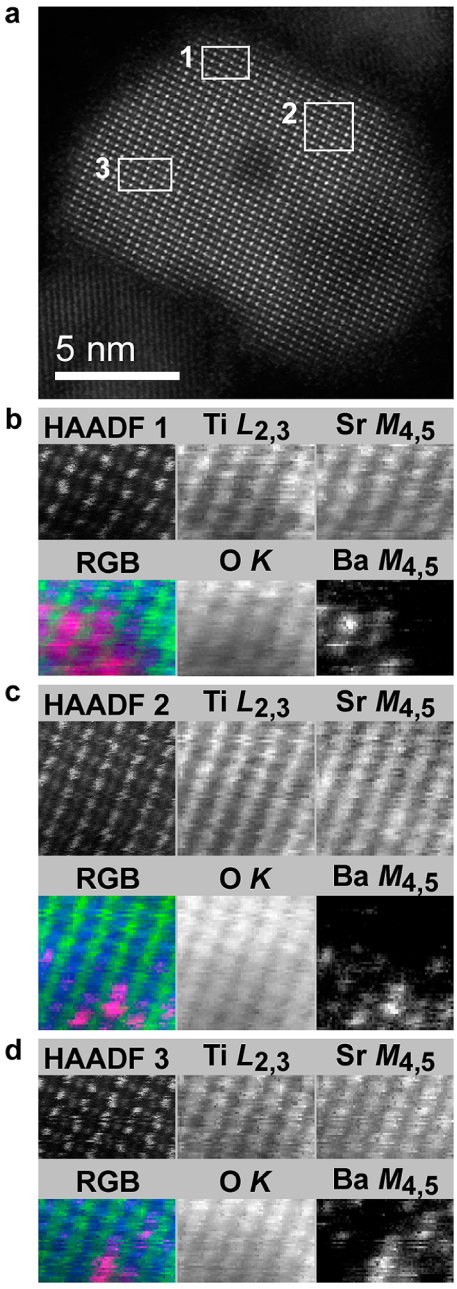

Figure 3. Spatial distribution of chemically identified Ba atoms in Ba-doped STO nanoparticles. (a) HAADF-STEM image of a Ba-doped STO nanoparticle along the [011] direction. (b–d) Simultaneous HAADF images and elemental atomic-resolution maps calculated from the EELS images obtained from areas 1–3 outlined with white squares in panel a. The RGB maps were generated using red for Ba, green for Ti, and blue for Sr.

to adjacent columns. To address this point, the role of electron channeling was explored by calculating EELS images of the Ba-$M_{4,5}$ edge based on the multislice theory. The contrast in atomic-resolution Ba-$M_{4,5}$ maps was reproduced by single-channeling simulations according to the experimental parameters on a 60 eV full energy window and on a single energy loss value 10 eV above threshold. For comparison, double-channeling calculations were also carried out;

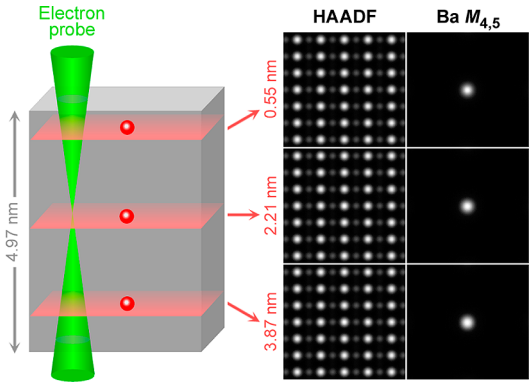

Figure 4. *Z*-contrast STEM and EELS simulations of the Ba-$M_{4,5}$ edge for a single Ba impurity. The Ba atom is embedded in a ~5 nm thick STO crystal oriented along [011]. Shown are double-channeling simulations obtained on a single energy loss value 10 eV above the threshold. Top, middle, and bottom rows correspond to simulations with the Ba atom located at a depth of 0.55, 2.21, and 3.87 nm, respectively (as depicted in the schematic drawing).

see Figure 4. Although the single channeling approximation neglects channeling of the fast electron after the core electron excitation, we find that the faster simulation approach produces qualitatively similar results to the double channeling method (see Supporting Information Figure S3).

Figure 4 shows the simulated maps of the Ba-$M_{4,5}$ edge for a Ba impurity embedded in a ~5 nm thick STO crystal. In these simulations an impurity was set at a depth of 0.55, 2.21, and 3.87 nm. As shown in Figure 4, the EELS signal of a single Ba atom is clearly localized on the respective atomic column regardless of the position of the Ba atom along the beam direction. We also explored the effect of sample mistilt away from the exact zone-axis conditions and simulations were obtained for 9.5 and 19 mrad tilt angles (see Supporting Information Figure S4). As expected for such thin crystals, the effects are very small and no delocalization of the ionization interaction is observed. On the basis of these calculations, we conclude that the inhomogeneous Ba distribution observed in the experimental EELS images is not an artifact of dynamical electron scattering and must therefore be attributed to the A-site clustering of Ba atoms.

A final question concerns the intensity differences in the Ba signal observed in Figure 3b–d. These intensity variations most probably arise either from Ba atoms located at different depths or from atomic columns containing different numbers of Ba atoms. Figure 5 shows STEM-EELS image simulations of a ~5 nm thick STO crystal containing Ba atoms in two different configurations. In Figure 5a, two Ba atoms are placed in two neighboring *A*-site columns spaced by 0.39 nm. The Ba atoms are separated 3.87 nm from each other along the electron beam direction. The corresponding EELS image of Figure 5b shows that the EELS signal of the Ba atom located at the entrance side of the electron

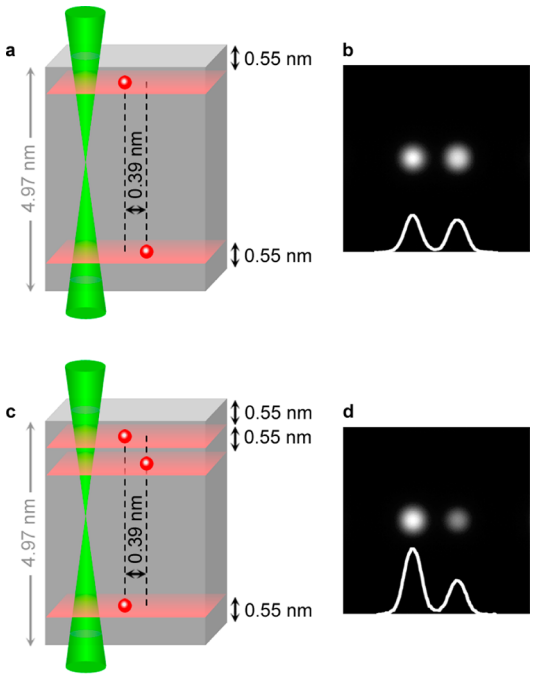

Figure 5. EELS simulations of the Ba-$M_{4,5}$ edge for several Ba impurities. (a, c) Schematic drawings of two different configurations of Ba atoms embedded in a ~5 nm thick STO crystal oriented along [011]. (b, d) EELS simulations of the Ba-$M_{4,5}$ edge for the configurations in panels a and c, respectively. Insets: horizontal line profiles extracted through the center of the Ba signals which are spaced by 0.39 nm. The single-channeling simulations assumed the full 60 eV energy window.

probe is only 15% brighter than the signal of the Ba atom located at the exit side. In Figure 5c, two Ba atoms separated 3.87 nm from each other are placed on the same atomic column, while a third one is located on a neighboring atomic column. For this configuration, the intensity rise of the Ba EELS signal for the atomic column containing two Ba atoms is ~90% compared to the one containing a single dopant atom; see Figure 5d. These differences are in good agreement with the intensity differences observed in the experimental Ba maps of Figure 3 indicating that the actual occupation of Ba atoms in individual atomic columns is the crucial factor for the observed EELS intensity. This provides further evidence for the presence of BTO clusters in STO nanoparticles. Yet, how does our observation of BTO clusters in nanoparticles relate to the known properties of Ba:STO?

The presence of polar nanoregions in $Ba_xSr_{1-x}TiO_3$ thin films was previously observed by near-field scanning optical microscopy[29] and Raman spectroscopy.[30] The reason for the occurrence of these polar nanoregions, however, remained unclear. Our observation of Ba-rich nanodomains in STO thus outlines a possible explanation for the presence of polar nanoregions in the Ba:STO system. This explanation is in line with the observation of polar nanoregions in the Ca:STO system which have generally been attributed to chemical heterogeneity; see for example, references 31 and 32. Yet, it still remains to be shown whether similar Ba-rich clusters also exist in Ba-doped STO films or whether they are characteristic for the nanoparticles only.

CONCLUSIONS

In summary, our results demonstrate that the combination of STEM-EELS and multivariate statistical analysis is a powerful tool to detect single dopant atoms, to determine the type of lattice site they occupy, and to map their distribution in nanoparticles with atomic resolution. By calculating EELS maps of Ba atoms in various configurations we have shown that the Ba $M_{4,5}$ core-loss signal is strongly localized on their respective atomic columns. This provides the theoretical base to conclude that the observed Ba dopant fluctuations in STO nanoparticles are real. These results could potentially relate to previous experimental[29] and theoretical[33] findings suggesting the existence of polar Ba-rich nanoregions in $Ba_xSr_{1-x}TiO_3$ thin films. We anticipate that the ability to chemically probe individual atoms and to determine their placement in nanodevices will provide new insights into the emerging field of solotronics (solitary dopant optoelectronics), where the essential element of a device is a single dopant atom.

METHODS

Synthesis of the Ba-Doped $SrTiO_3$ Nanoparticles. Crystalline $Ba_{0.03}Sr_{0.97}TiO_3$ nanoparticles were obtained employing a nonhydrolytic and halide-free procedure.[28] The reaction mixture was prepared in a glovebox with argon atmosphere. In the first step of the procedure a stoichiometric amount of metallic barium and strontium was dissolved in anhydrous benzyl alcohol at 80 °C. The resulting solution was mixed with 1 mol equiv of titanium isopropoxide, and the reaction mixture was transferred to a 45 mL Teflon-lined stainless steel autoclave (Parr acid digestion bombs). After sealing, the autoclave was removed from the glovebox and heated at 200 °C for 48 h. The precipitate was extracted by centrifugation and washed several times with ethanol. Finally, the nanoparticles were dispersed in ethanol by ultrasonication and a drop of the suspension was air-dried onto a carbon-coated copper grid for TEM characterization. Before loading the samples into the microscope, they were either plasma cleaned for a few seconds or heated under vacuum at 100 °C to remove hydrocarbon contamination from the surfaces of the nanocrystals.

Instrumentation. HAADF-STEM was performed using a JEOL 2200FS TEM/STEM microscope operated at 200 kV. Considering the spherical aberration C_S of 1 mm, the probe semiconvergence angle was 10.8 mrad and the inner semidetection angle of the annular dark field detector was calibrated at 100 mrad. For these operating conditions, the microscope provides a spatial resolution of about 1.6 Å. The EELS data in this study was obtained at 100 kV on a NION UltraSTEM 100 microscope equipped with a C_5 NION quadrupole–octupole-type probe aberration corrector and an ultrahigh vacuum Gatan Enfina spectrometer. The convergence and collection semiangles were set to 30.5 and 33 mrad, respectively. For these values,

the energy resolution measured as the full width at half-maximum of the zero-loss peak is ~0.35 eV. Yet, in order to cover a large energy range in EELS, the dispersion was set to 1 eV/channel which implies that the actual energy resolution of the EELS measurements is given by the point-spread function of the spectrometer's channel detector. The energy windows used to form the EELS images are 120, 35, 30, 60, and 32 eV for the Sr-$M_{4,5}$, Ti-$L_{2,3}$, O-*K*, Ba-$M_{4,5}$ and Ba-$N_{4,5}$ edges, respectively. In typical operating conditions for the experiments described in this paper, the microscope provides an estimated spatial resolution of 0.85 Å allowing for a depth of field between 4 and 8 nm. The annular semidetection range of the annular dark-field detector was set to collect electrons scattered between 95 and 195 mrad.

Image Simulations. High-resolution STEM image simulations in Figures 1 and 2 were carried out using the *x*HREM simulation package while the structural models used for the HAADF-STEM image simulations were built using the CrystalKit (TotalResolution) software. Atomic resolution 2D EELS maps of the Ba-$M_{4,5}$ edge were calculated using single- and double-channeling simulations[34] according to the experimental parameters of the probe-forming lens and the detector collection geometry. The defocus value was chosen to position the beam waist near the center of the nanoparticle since this maximized the HAADF image contrast, the method used to select the defocus value during the experiment. Single-channeling calculations were performed for both a 60 eV full energy window and on a single energy loss value 10 eV above threshold, while the double-channeling calculations were performed for the single 10 eV energy loss value only. The energy loss window calculations were performed following the approach of Allen *et al.*[35] while the single energy loss calculations were performed following the approach of Dwyer,[36] both within a multislice formulation. Spatial incoherence was accounted for by convolving with a Gaussian with half width at half-maximum of 0.04 nm. The structural models used for the calculations were built by simply substituting Ba for Sr in a perfect, periodic STO structure, that is, no structural relaxation was attempted. Debye–Waller factors for STO were obtained from the literature,[37] and the Debye–Waller factor for Ba was set equal to that for Sr (modest variations in this choice made no qualitative difference to the calculations).

Conflict of Interest: The authors declare no competing financial interest.

Supporting Information Available: Additional figures showing experimental and calculated atomic resolution 2D EELS maps. This material is available free of charge *via* the Internet at http://pubs.acs.org.

Acknowledgment. We acknowledge the financial support of the Swiss COST office under the SBF project number C10.0089 and of ETH Zurich. S.D.F. acknowledges support by the Australian Research Council. The SuperSTEM Laboratory is supported by the U.K. Engineering and Physical Sciences Research Council (EPSRC).

REFERENCES AND NOTES

1. Chen, W.; Zhanf, J. Z.; Joly, A. G. Optical Properties and Potential Applications of Doped Semiconductor Nanoparticles. *J. Nanosci. Nanotechnol.* **2004**, *4*, 919–947.
2. Norris, D. J.; Efros, A. L.; Erwin, S. C. Doped Nanocrystals. *Science* **2008**, *319*, 1776–1779.
3. Bryan, J. D.; Gamelin, D. R. Doped Semiconductor Nanocrystals: Synthesis, Characterization, Physical Properties, and Applications. *Prog. Inorg. Chem.* **2005**, *54*, 47–126.
4. Koenraad, P. M.; Flatté, M. E. Single Dopants in Semiconductors. *Nat. Mater.* **2011**, *10*, 91–100.
5. Voyles, P. M.; Muller, D. A.; Grazul, J. L.; Citrin, P. H.; Gossmann, H.-J. L. Atomic-Scale Imaging of Individual Dopant Atoms and Clusters in Highly *n*-Type Bulk Si. *Nature* **2002**, *416*, 826–829.
6. Kaiser, U.; Muller, D. A.; Grazul, J. L.; Chuvilin, A.; Kawasaki, M. Direct Observation of Defect-Mediated Cluster Nucleation. *Nat. Mater.* **2002**, *1*, 102–105.
7. Erni, R.; Heinrich, H.; Kostorz, G. Quantitative Characterization of Chemical Inhomogeneities in Al–Ag Using High-Resolution *Z* Contrast STEM. *Ultramicroscopy* **2003**, *94*, 125–133.
8. Oh, S. H.; van Benthem, K.; Molina, S. I.; Borisevich, A. Y.; Luo, W.; Werner, P.; Zakharov, N. D.; Kumar, D.; Pantelides, S. T.; Pennycook, S. J. Point Defect Configurations of Supersaturated Au Atoms inside Si Nanowires. *Nano Lett.* **2008**, *8*, 1016–1019.
9. Okuno, H.; Rouvière, J.-L.; Jouneau, P.-H.; Bayle-Guillemaud, P.; Daudin, B. Visualization of Tm Dopant Atoms Diffused out of GaN Quantum Dots. *Appl. Phys. Lett.* **2010**, *96*, 251908.
10. Couillard, M.; Radtke, G.; Knights, A. P.; Botton, G. A. Three-Dimensional Atomic Structure of Metastable Nanoclusters in Doped Semiconductors. *Phys. Rev. Lett.* **2011**, *107*, 186104.
11. Van Aert, S.; Batenburg, K. J.; Rossell, M. D.; Erni, R.; Van Tendeloo, G. Three-Dimensional Atomic Imaging of Crystalline Nanoparticles. *Nature* **2011**, *470*, 374–377.
12. Bar-Sadan, M.; Barthel, J.; Shtrikman, H.; Houben, L. Direct Imaging of Single Au Atoms within GaAs Nanowires. *Nano Lett.* **2012**, *12*, 2352–2356.
13. Shibata, N.; Findlay, S. D.; Azuma, A.; Mizoguchi, T.; Yamamoto, T.; Ikuhara, Y. Atomic-Scale Imaging of Individual Dopant Atoms in a Buried Interface. *Nat. Mater.* **2009**, *8*, 654–658.
14. Krivanek, O. L.; Chisholm, M. F.; Nicolosi, V.; Pennycook, T. J.; Corbin, G. J.; Dellby, N.; Murfitt, M. F.; Own, C. S.; Szilagyi, Z. S.; Oxley, M. P.; *et al.* Atom-by-Atom Structural and Chemical Analysis by Annular Dark-Field Electron Microscopy. *Nature* **2010**, *646*, 571–574.
15. Ortalan, V.; Uzun, A.; Gates, B. C.; Browning, N. Direct Imaging of Single Metal Atoms and Clusters in the Pores of Dealuminated HY Zeolite. *Nat. Nanotechnol.* **2010**, *5*, 506–510.
16. Aydin, C.; Lu, J.; Liang, A. J.; Chen, C.-Y.; Browning, N.; Gates, B. C. Tracking Iridium Atoms with Electron Microscopy: First Steps of Metal Nanocluster Formation in One-Dimensional Zeolite Channels. *Nano Lett.* **2011**, *11*, 5537–5541.
17. Browning, N. D.; Chisholm, M. F.; Pennycook, S. J. Atomic-Resolution Chemical Analysis Using a Scanning Transmission Electron Microscope. *Nature* **1993**, *366*, 143–146.
18. Varela, M.; Findlay, S. D.; Lupini, A. R.; Christen, H. M.; Borisevich, A. Y.; Dellby, N.; Krivanek, O. I.; Nellist, P. D.; Oxley, M. P.; Allen, L. J.; Pennycook, S. J. Spectroscopic Imaging of Single Atoms within a Bulk Solid. *Phys. Rev. Lett.* **2004**, *92*, 095502.
19. Okunishi, E.; Sawada, H.; Kondo, Y.; Kersker, M. Atomic Resolution Elemental Map of EELS with a Cs Corrected STEM. *Microsc. Microanal.* **2006**, *12*), 1150–1151.
20. Kimoto, K.; Asaka, T.; Nagai, T.; Saito, M.; Matsui, Y.; Ishizuka, K. Element-Selective Imaging of Atomic Columns in a Crystal Using STEM and EELS. *Nature* **2007**, *450*, 702–704.
21. Bosman, M.; Keast, V. J.; García-Muñoz, J. L.; D'Alfonso, A. J.; Findlay, S. D.; Allen, L. J. Two-Dimensional Mapping of Chemical Information at Atomic Resolution. *Phys. Rev. Lett.* **2007**, *99*, 086102.
22. Muller, D. A.; Kourkoutis, L. F.; Murfitt, M.; Song, J. H.; Hwang, H. Y.; Silcox, J.; Dellby, N.; Krivanek, O. L. Atomic-Scale Chemical Imaging of Composition and Bonding by Aberration-Corrected Microscopy. *Science* **2008**, *319*, 1073–1076.
23. Gunawan, A. A.; Mkhoyan, K. A.; Wills, A. W.; Thomas, M. G.; Norris, D. J. Imaging "Invisible" Dopant Atoms in Semiconductor Nanocrystals. *Nano Lett.* **2011**, *11*, 5553–5557.
24. Watanabe, M.; Okunishi, E.; Ishizuka, K. Analysis of Spectrum-Imaging Datasets in Atomic-Resolution Electron Microscopy. *Microsc. Anal.* **2009**, *23*, 5–7.
25. Barrett, J. H. Dielectric Constant in Perovskite Type Crystals. *Phys. Rev.* **1952**, *86*, 118–120.
26. Müller, K. A.; Burkard, H. $SrTiO_3$: An Intrinsic Quantum Paraelectric below 4 K. *Phys. Rev. B* **1979**, *19*, 3593–3602.
27. Hemberger, J.; Nicklas, M.; Viana, R.; Lunkenheimer, P.; Loidl, A.; Böhmer, R. Quantum Paraelectric and Induced

Ferroelectric States in $SrTiO_3$. *J. Phys.: Condens. Matter* **1996**, *8*, 4673–4690.
28. Niederberger, M.; Garnweitner, G.; Pinna, N.; Antonietti, M. Nonaqueous and Halide-free Route to Crystalline $BaTiO_3$, $SrTiO_3$, and $(BaSr)TiO_3$ Nanoparticles *via* a Mechanism Involving C−C Bond Formation. *J. Am. Chem. Soc.* **2004**, *126*, 9120–9126.
29. Hubert, C.; Levy, J. Nanometer-Scale Imaging of Domains in Ferrolectric Thin Films Using Apertureless Near-Field Scanning Optical Microscopy. *Appl. Phys. Lett.* **1998**, *73*, 3229–3231.
30. Tenne, D. A.; Soukiassian, A.; Zhu, M. H.; Clark., A. M.; Xi, X. X.; Choosuwan, H.; He, Q.; Guo, R.; Bhalla, A. S. Raman Study of $Ba_xSr_{1-x}TiO_3$ Films: Evidence for the Existence of Polar Nanoregions. *Phys. Rev. B* **2003**, *67*, 012302.
31. Kleemann, W.; Dec, J.; Wang, Y. G.; Lehnen, P.; Prosandeev, S. A. Phase Transitions and Relaxor Properties of Doped Quantum Paraelectrics. *J. Phys. Chem. Solids* **2000**, *61*, 167–176.
32. Ranjan, R.; Pandey, D.; Lalla, N. P. Novel Features of $Sr_{1-x}Ca_xTiO_3$ Phase Diagram: Evidence for Competing Antiferroelectric and Ferroelectric Interactions. *Phys. Rev. Lett.* **2000**, *84*, 3726–3729.
33. Fuks, D.; Dorfman, S.; Piskunov, S.; Kotomin, E. A. *Ab Initio* Thermodynamics of $Ba_cSr_{(1-c)}TiO_3$ Solid Solutions. *Phys. Rev. B* **2005**, *71*, 014111.
34. Dwyer, C.; Findlay, S. D.; Allen, L. J. Multiple Elastic Scattering of Core-Loss Electron in Atomic Resolution Imaging. *Phys. Rev. B* **2008**, *77*, 184107.
35. Allen, L. J.; Findlay, S. D.; Oxley, M. P.; Rossouw, C. J. Lattice-Resolution Contrast from a Focused Coherent Electron Probe. *Ultramicroscopy* **2003**, *96*, 47–63.
36. Dwyer, C. Multislice Theory of Fast Electron Scattering Incorporating Atomic Inner-Shell Ionization. *Ultramicroscopy* **2005**, *104*, 141–151.
37. Peng, L. M. Anisotropic Thermal Vibrations and Dynamical Electron Diffraction by Crystals. *Acta Crystallogr., Sect. A* **1997**, *53*, 663–672.